2023 IEEE/ASME International Conference on Advanced Intelligent Mechatronics (AIM)
June 28-30, 2023. Seattle, Washington, USA

Mitigate Inertia for Wrist and Forearm Towards Safe Interaction in 5-DOF Cable-Driven Robot Arm

Van Pho Nguyen, Sunil Bohra Dhyan, Chi Cuong Hoang,
Boon Siew Han, Jing Yuan Tan, and Wai Tuck Chow*

***Abstract*— Demand of a lightweight robot arm for dexterously handling objects or working with low inertia has become a new challenge in robotics. This paper comes up with a novel design of a low-inertia robot arm comprising of 5 degrees of freedom (DOF) with 2 DOF at the wrist, 1 DOF at the elbow, 1 DOF at the shoulder, and 1 DOF at the base. The wrist is driven by a cable system, concurrently, all five motors actuating the robot arm locate near a shoulder center with a counterbalanced design. A novel design of a decoupling mechanism without spring components was proposed to enhance the stability of the wrist during loading heavy load. Experimental outcomes showed that our robot arm can lift 5 kg hooked at a long arm, and the accuracy in operating for the arm and the wrist reached smaller than 1 mm. This design is expected to generate a low-inertia robot arm for safe interactions and mobile applications. Our design targets to reduce the payload ratio to 1:1 with the arm weight being 5 kg and the lifetime durability of at least 6 months.**

I. INTRODUCTION

In today's market, there are numerous types of robot arms available, used predominantly in manipulation [1]–[5], the healthcare sector [6]–[8], and industrial production: welding, assembly [9]–[13]. Most of these robot arms created are rigid robot arms actuated using heavy stepper motors placed at the joints which allow for precise action of the end-effector [9]–[13]. For instance, the UR5 robot arm designed by Universal Robots (see Fig. 1), is a collaborative industrial robot arm with 6 Degrees of Freedom (DOF) and a reach of 0.85m [9]. It has a weight of 20.6kg and can lift payloads up to 5kg making the weight-to-payload ratio approximately 4:1. Although it has an accuracy of 0.1mm, the wrist of the robot arm is bulky making it difficult to carry heavier objects with the same motor power. Moreover, the system has a high moment of inertia posing a safety concern for humans working with them.

The shortcomings of the traditional rigid robots are overcome by soft robots which are made of soft-stretchable material like elastic silicone or dielectric elastomer (DE) [14]. Other robot hands with their soft body actuated by pneumatic [15]–[18]. These robots are lightweight and provide for good safety, adaptability, and flexibility. However, soft robots tend to have lower control over accuracy.

Nguyen, Dhyan, and Chow are at School of Mechanical and Aerospace Engineering, Nanyang Technological University, Singapore. Also, Nguyen and Dhyan are working with Hoang, Han, and Tan at Schaeffler Hub for Advanced Research at NTU. Email: ngvphobk08@gmail.com, {sunilbohra.dhyan, wtchow}@ntu.edu.sg. *: *corresponding author.*

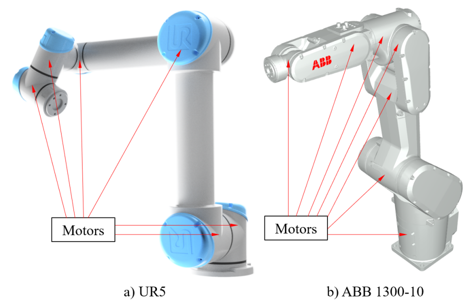

Fig. 1. The robot arms with the motors located at each joint in two showcases: a) UR5 and b) ABB 1300-10.

A. Related Works

Cable-actuated robots are another type of robots where the rigid links are replaced by wires or cables. This reduces the weight of the robot significantly and allows for achieving higher accelerations in workspaces [19], [20]. Moreover, by placement of actuators proximal to the base makes the robot more compact and with significantly lower inertia. This makes the human-robot interaction much safer in applications. The drawbacks of the robot are lower accuracy and high vibrations [21]. AMBIDEX is one such robot with 7DOF – 3 at the shoulder, 1 elbow, and 3 at the wrist. The joints are actuated using cables driven by electric motors and the system is designed for high-speed safe interaction [22]. However, due to the complicated design of the arm, there is very limited space for adding the bearings and sensor to reduce friction and enhance the working accuracy. Additionally, the design of the wrist is complicated and bulky for carrying payloads, especially in bearing lateral load.

B. Research concept

To overcome the given problem, we propose a novel design of a cable-driven robot arm having light body weight, low operating inertia, and can bear heavy load. In this scenario, the robot arm has 5 DOF and comprises of the wrist, the forearm, the elbow, the upper arm, the shoulder, and the base (see Fig. 1). The rotational motions of the wrist are driven by the Dyneema cables, concurrently, all motors locate near the shoulder to counterbalance the load hooked at the wrist. The novelty points of our research include:

- Robot arm: Proposes a novel 5-DOFs robot arm that can handle heavy torque (lifts 5kg load hooked at the wrist's free end 500mm distance from the elbow joint). Reduces energy consumption of the robot arm and the power of the shoulder motor by the counterbalance design.

- Elbow movement: Reduces the bulky structure of the elbow by using only one hinge for the elbow joint. Additionally, increases the accuracy and stability of the elbow movement by a 3-link parallel mechanism.
- Design a novel decoupling mechanism that can keep unchanged the cable tension when the forearm rotates around the elbow joint.

II. DESIGN OF ROBOT ARM

In Fig. 2, the robot arm comprises the main clusters such as the wrist, forearm, elbow, upper arm, and base. Such clusters join with the others by the hinge joins or rotational structures that form the correlating motions for the robot arm. If we set up the coordinate systems at each joint as shown in Fig. 2a), the robot arm comprises 5 degrees of freedom (DOF): 2 DOF at the wrist (rotates θ_{x4}, θ_{z4}), 1 DOF at the elbow (rotates θ_{z3}), 1 DOF at the shoulder (rotates θ_{z2}) and 1 DOF at the base (rotates θ_{z1}).

A. Robot frame

In Fig. 3, the robot frame consists of six main panels divided into three pairs with parallel structures at the forearm, the upper arm, and the base. In this scenario, the pair of panels at the base (aka the base panels) are firmly spaced at their bottom by the connecting plates including two vertical plates and two horizontal plates mounted as a box. Also, the horizon plates are directly fixed to the RMD-X10 motor whose shaft is locked to a jig block. Hence, the entire base and the motor can rotate around the axis z_1, concurrently, the motor shaft of RMD-X10 is stationary.

The top of the base panels is firmly spaced by the shoulder joint (z_2, θ_{z2}) which generates the rotational motion between the upper arm and the base. The distance between the center line of the shoulder joint and the floor is 426 mm. In this design, the upper arm plays the most important role in the arm where four motors are located on its main panels. Among those, one RMD-X10 motor (aka shoulder motor M_S) is located at the RH-upper panel where its motor shaft is directly fixed to the RH-base panel and coincident with the shoulder joint. In Fig. 2c) the RMD-X10 motor (aka elbow motor M_E) is far a distance of 179 mm on the right-hand side from the shoulder joint and mounted on the same panel with M_S. One end of the driving bar is attached to the motor shaft of M_E, concurrently its remaining end links with a connecting rod through a hinge joint. Two RMD-X6 motors (aka RH-Wrist motor M_{RW} and LH-Wrist motors M_{LW}) locate on the LH-Upper panel and on the right-hand side of the shoulder joint. Each motor shaft of these two motors affixes one cable tightening mechanism to terminate the cable ending and maintain the cable tension. In this situation, one cable tightening mechanism takes over one pair of cable branches which drives the motions of one wrist pulley.

The elbow is a hinge joint located at a distance of 400 mm from the left-hand side of the shoulder joint. The main structure of the elbow allows the forearm panels and the

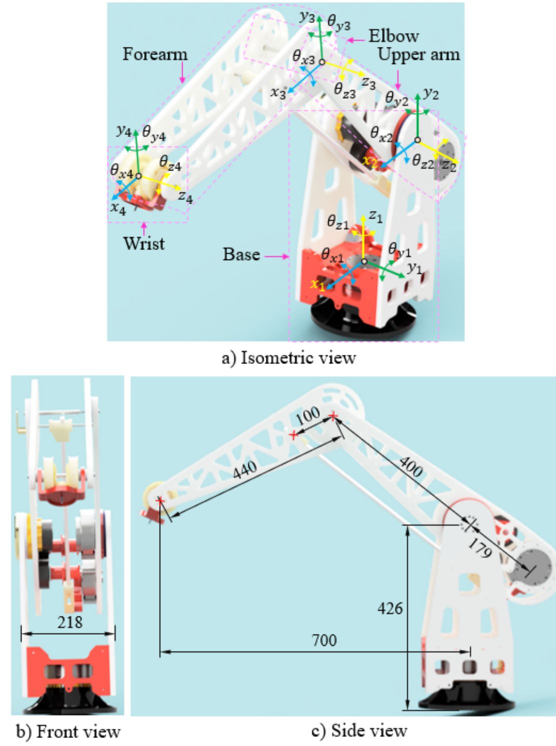

Fig. 2. 3D design of the cable-driven robot arm with different views: a) isometric view, b) front view, and c) side view. Inside the boxes surrounded by pink-dash lines display the structures of the main clusters in the cable-driven robot arm.

upper arm panels to rotate around an elbow shaft. Such panels are mounted in two pairs on the RH- and LH-side. On the elbow shaft and between the forearm panels, four elbow pulleys (p_1, p_2, p_3, p_4) are assembled to bear the cables ($c1, c2, c3, c4$) with each cable on one pulley. According to this design, the elbow becomes more compact because the multiple links and joints in [22] are completely replaced by a hinge joint. Technically, this design reduces assembly errors and allows us to mount the encoder for precisely tracking the rotational motion of the forearm around the elbow joint. The encoder continuously returns feedback to the elbow motor for precisely controlling the rotational angle of the forearm.

The forearm includes two symmetrical panels with three hinge joints: at the elbow, at the wrist, and at the forearm shaft (with the center line S_F). In this design, S_F places on the center line of the RH- and LH-forearm panels and has a 100 mm distance from the elbow center line (aka S_E). On the forearm shaft, a block is used to terminate an ending of the connecting rod. Hence, four points S_F, S_E, S_{ME}, S_{CD} form a parallelogram shape. In other words, the forearm, the upper arm, the driving bar, and the connecting rod can carry out two parallel motions as the motor M_S rotates. This parallelogram mechanism enhances the stiffness and accuracy of the forearm when it moves around the elbow joints. In particular, it increases the bearing capability of the long forearm with 440 mm distance between the wrist hinge joint (S_W) and the elbow hinge joint (S_E).

The robot frame with V-shape panels bonded by the network of lateral connecting shafts can enhance the capability of bearing the external force and torque even if the length of the arm becomes significantly longer. The V-shape design facilitates in optimizing the frame shape and reducing the weight of the robot body. Additionally, fabricating the frame and locating the components inside the arm becomes simpler. This saves fabricating time, simplifies machining, and reduces costs.

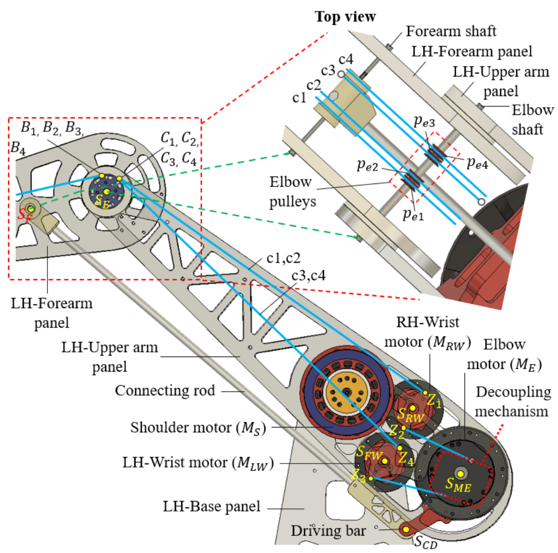

Fig. 3. Schematic illustration of the robot frame. The inset image inside the dash-red box shows the structure of the robot arm at the elbow joint. Also, the blue lines are the visualizations of the cables, concurrently, the green-dash arrows link the shafts between two image views.

B. Wrist

The wrist locates at one end of the forearm and has two rotational motions around axes x_4, z_4 as shown in Fig. 4. Such motions of the wrist are driven by a differential gear mechanism comprising two symmetrical-ring gears and one pinion gear. The ring shaft is the center shaft of the wrist hinge joint (between the wrist and the forearm panels) and the ring gears. The bore of each ring gear has hole and groove structures that facilitate locking the middle area of one cable. From this locking structure, the cable forms two branches (aka branches: *c1*, *c2* on the RH-Wrist pulley) and *c3*, *c4* on the LH-Wrist pulley) to drive two rotational directions of the wrist pulleys. Also, to enhance the durability of locking the cable, such cable branches are wound on the pulley bore at least three turns for each. The cable branches *c1,c2,c3,c4* lean on the elbow pulleys $p_{e1}, p_{e2}, p_{e3}, p_{e4}$, decoupling mechanism, and terminate at the tightening mechanism fixed at the M_{RW}, M_{LW} motors. In this research, two Dyneema cables are used to drive those wrist pulleys with the main principle: pull one branch and simultaneously release the remaining branch with the constant cable length. As controlling the Dyneema cables, the correlative rotations between the ring gears rotate the pinion-bevel gear in θ_{x4} direction. Simultaneously, depending on the velocity of two wrist pulleys, the pinion shaft is stationary or rotates in θ_{z4} direction. The differential gear mechanism also enhances the accuracy and stability of the wrist motions. Moreover, it benefits mounting a sensor system for precisely tracking the motions of the wrist.

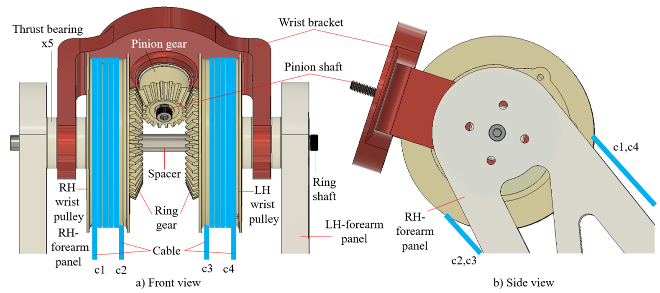

Fig. 4. The wrist design with a) front view and b) side view.

C. Decoupling Mechanism

Basically, two ends of one cable branch in group *c1,c2,c3,c4* are fixedly mounted on the wrist pulley and the tightening mechanism, whereas their middle lengths have to lean on the elbow pulleys. This mounting way can be illustrated in Fig. 5 for the cable branch *c1*. When the angle between the forearm and the upper arm (or $S_W\widehat{S_E, S}_{ME}$) varies with an amount $d\theta_{z3}$, B_1 changes. This leads to a different length of *c1* (aka Δl_{c1}) compared with its initial length. From the geometrical calculation in Fig. 5, Δl_{c1} equals to $r_e d\theta_{z3}$. In other words, the different length of *c1* is proportional to the angle $d\theta_{z3}$ in the structure with the unchanged diameter of the elbow pulley. If there is no compensation for eliminating Δl_{c1}, the tension inside the cable *c1* is unstable which causes low accuracy in operation and cable loosening.

To overcome this problem, the cable branch *c2* additionally leans on a decoupling mechanism located between the elbow pulley and the tightening mechanism. In Fig. 5, the decoupling mechanism consists of three pulleys: a minor-compensating pulley having the same center S_{ME} with a big-compensating pulley, and a guiding pulley (center S_G). Such pulleys freely rotate around their shafts, concurrently, link $S_{ME}S_G$ and the driving bar is fixed together as one rigid part. Also, the radius r_b is designed with exactly three folds bigger than r_m ($r_m = r_e$). The mounting trajectory of the branch *c1* and *c2* are $A_1 \rightarrow B_1 \rightarrow C_1 \rightarrow Z_1$ and $A_2 \rightarrow B_2 \rightarrow C_2 \rightarrow D_2 \rightarrow E_2 \rightarrow F_2 \rightarrow G_2 \rightarrow H_2 \rightarrow I_2 \rightarrow Z_2$, respectively. According to this mechanism, when the driving bar clockwise rotates an $d\theta_{z3}$ angle, the length of branches *c1* and *c2* reduces an amount of $d\theta_{z3}r_e$ and $d\theta_{z3}(r_e + r_m) = 2d\theta_{z3}r_e$ at the position where the cables contact the elbow pulleys and the minor-compensating pulley. Simultaneously, at the contact position between *c2* and the big-compensating pulley, only the length of *c2* increases an amount of $d\theta_{z3}r_b = 3d\theta_{z3}r_e$. To balance the length of *c1* and *c2*, the tightening pulley rotates an angle $d\theta_{z3}r_e/r_w$ in the clockwise direction. This decoupling mechanism significantly restricts the error in operation caused by using the spring systems. Hence, the cables can achieve high stability as the robot arm loads heavy loads. Then, this decoupling mechanism is also replicated to mount the cable branches *c3,c4*.

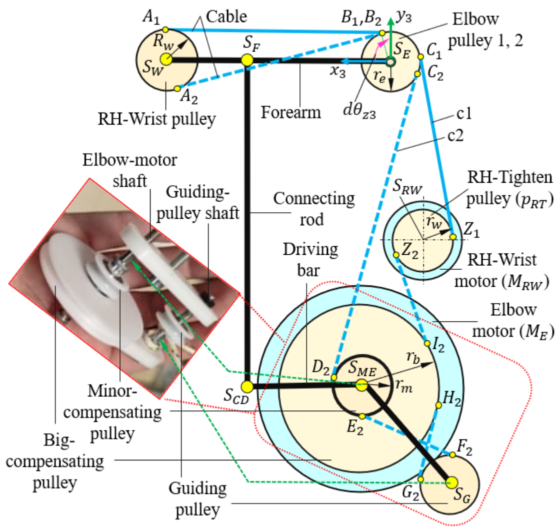

Fig. 5. Illustration of the decoupling mechanism. The inset image shows the fabricated-decoupling mechanism. The bold-black links represent the parallelogram mechanism in Fig. 3, concurrently, the solid- and dash-blue curves denote the cable branches: *c1*, and *c2*, respectively. This mechanism is also applied to the cable branches: *c3*, and *c4* in the same order. Also, B_1, C_1, Z_1 and $B_2, C_2, D_2, E_2, F_2, G_2, H_2, I_2$ are the points starting/ending the contacts between the cable branch *c1*, and *c2*, respectively.

III. RESULTS

A. Fabrication

As shown in Fig. 6, the panels were made from PLA plastic printed by AnyCubic 3D printer. The differential gear wrist mechanism is comprised of a set of 3 plastic bevel gears with strong stiffness for bearing the heavy load. The connecting rod was a lightweight tube with a cross-section of 8×10 mm diameter and was made from Carbon fiber composite material. The cables used in this fabrication were Dyneema type with a diameter of 2 mm.

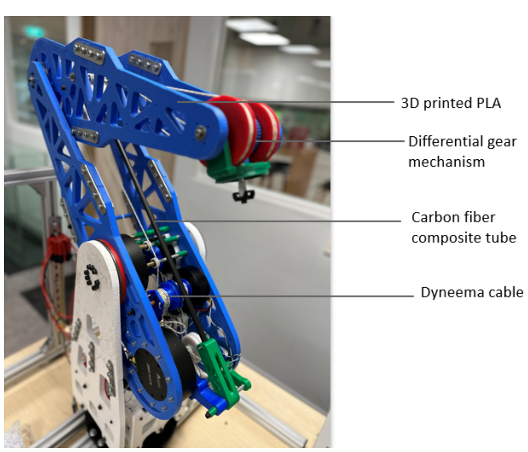

Fig. 6. Schematic illustration of the experimental Setup for 5-DOF Cable-driven Robot Arm.

B. Electrical design and controlling the robot arm

The actuation unit of the robot arm consists of five RMD-X Series high precision, compact pancake servo motors (see Fig. 7). The shoulder and elbow actuation unit jointly comprises three RMD-X10 motors with a gear ratio of 1:7, and the wrist actuation unit comprises two RMD-X6 motors with a gear ratio of 1:6. The motors require a nominal voltage of 48V to achieve the desired torque required to carry out the operations of the robot arm. The motors use a High-speed CAN bus network to establish communication with each other and the network runs at a speed of 500Kbps.

An end of the CAN bus network is connected to a CAN Host Computer which is used to send commands and data packages to the CAN network to allow the motors to perform specific functions. The program is scripted in the Arduino interface which in turn is compiled and uploaded onto the CAN network. Lastly, to facilitate communication over the network the two ends of the CAN bus require a terminal resistance of 120Ω connected in parallel, resulting in the overall network resistance to be 60Ω. The overall setup can be visualized as shown in Fig. 7.

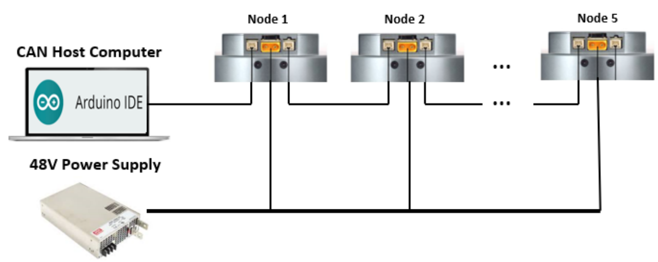

Fig. 7. Schematic illustration of the experimental Setup for 5-DOF Cable-driven Robot Arm.

C. Loading test

The loading test for the cable-driven robot arm was divided into two components (1) Load Test for the shoulder and elbow, and (2) Load Test for the wrist. The loads used in the test were 1 kg rice bags each.

1) Load Test for shoulder and elbow: The shoulder and elbow motors of the robot arm lifted the payload from position A to position B (see Fig. 8). At 1kg payload, for the robot arm to reach position B from position A, the elbow motor required a velocity of 7.5 rpm. As the payload value increased, to compensate for the increasing weight, the output velocity of the elbow motor had to be increased consequently. As shown in Fig. 9 for 2 kg, 3 kg, 4 kg and 5 kg payload, the motor required increasing velocities of 33.34 rpm, 55 rpm, 66.67 rpm and 83.34 rpm respectively.

2) Load Test for wrist: In the wrist load test, we loaded the wrist of the robot arm with 4 kg and 5 kg payload. The wrist of the robot arm was able to lift the loads from the home position of the wrist to clockwise -90° and, counter-clockwise +90° as shown in Fig. 10.

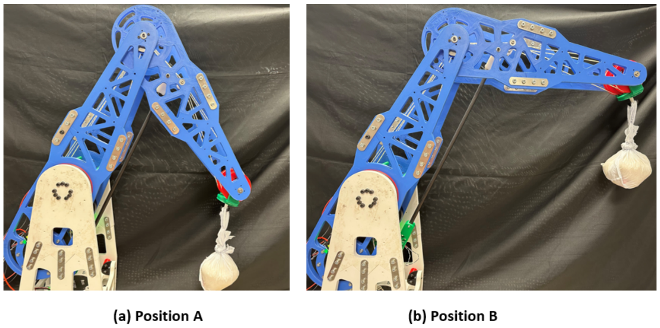

Fig. 8. Experiment showing Elbow load test at Position A and B.

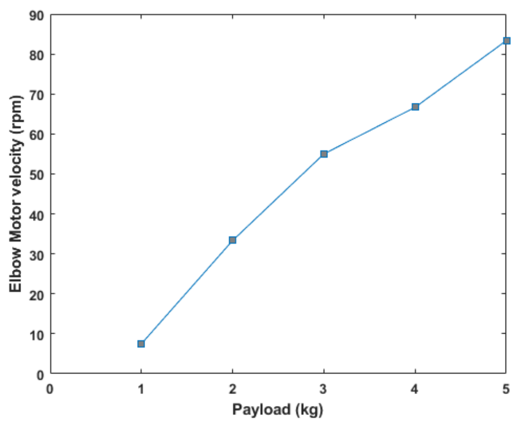

Fig. 9. Graphical illustration of the output elbow-motor velocity versus payload at robot wrist.

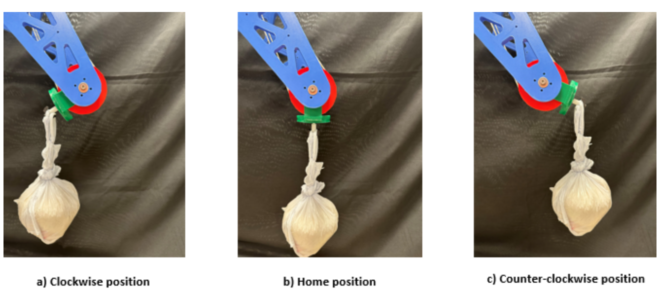

Fig. 10. Experiment showcasing Wrist load tests with payloads of 4kg and 5kg at configurations: a) -90° b) 0° c) +90°.

D. Accuracy test

Accuracy is one of the main measurable characteristics of robot arms as it has a direct impact on the application and effectiveness of robots during the completion of tasks. The accuracy of robot arms can be broken down into pose accuracy and path accuracy. In this section of the paper, our focus is only on the static characteristics, hence we focus on the pose accuracy. The pose accuracy is further broken down into positional and orientation accuracy. In our experiments, we measure the absolute position accuracy of the robot arm. Absolute here refers to the position accuracy with respect to the global reference frame. Experiments were conducted to measure the accuracy of the robot arm over 5 trials. In Fig. 11 a dial gauge indicator with a magnetic base was mounted on a metal platform. The robot arm was programmed to actuate itself towards the tip of the dial gauge, just enough to obtain readings from the gauge indicator.

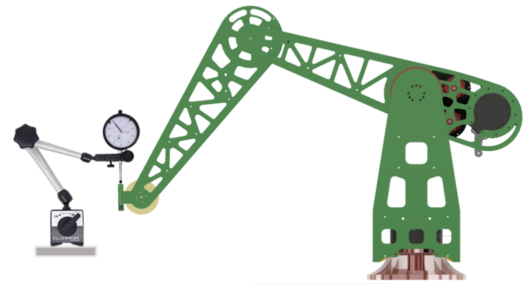

Fig. 11. Schematic illustration of the experimental setup to measure the accuracy of the cable-driven robot arm.

The above-mentioned experiments were broken down into 4 separate tests to determine the accuracy at each joint/ DOF: (a) LH-Wrist (b) RH-Wrist (c) Both wrists combined (d) 4-DOFs (2 wrist, 1 elbow, 1 shoulder). The readings obtained from the dial gauge indicator are tabulated in Table I.

TABLE I
ACCURACY TEST DIAL GAUGE INDICATOR READING (UNIT MM)

LH-Wrist	RH-Wrist	Both Wrists	4-DOF
0.28	0.65	0.38	0.18
0.24	0.72	0.38	0.18
0.24	0.65	0.38	0.14
0.24	0.63	0.38	0.1
0.23	0.63	0.38	0.07

The above data shown in the table is illustrated in a graphical format in Fig. 12 to make it more intuitive for the readers. As observed from the line plot, the maximum deviation in dial gauge readings is for 4-DOF motion of the robot arm with its range being 0.11 mm, on the other hand the minimum deviation in readings is for both wrists combined whose range is 0 mm. The range of readings for the LH-Wrist is 0.05 mm, and that of the RH-Wrist is 0.09 mm.

In Fig. 13 the standard deviation of the dial gauge readings is plotted to determine the accuracy of each joint. The standard deviation for both wrists is zero, thus using both wrists operated by 4 pairs of Dyneema cables is the most accurate. While just using the LH-Wrist independently the standard deviation is 0.019 mm, whereas for the RH-Wrist is 0.037 mm. From the plot, it can be observed that during the motion of all 4-DOFs, the accuracy is the minimum as the standard deviation is 0.049 mm, the maximum. Hence, we can infer that the errors occur mostly at the shoulder and elbow joints.

In future works, we aim to attach sensors to track the motion of the elbow and wrist. Hence, the working accuracy of the robot arm would be improved. Also, the weight of this robot arm is concerned to reduce from 7.5 kg to 5 kg by

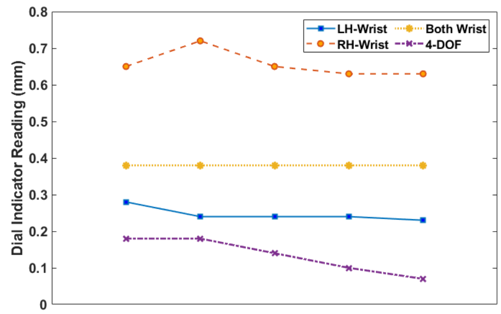

Fig. 12. Graphical illustration of Dial gauge indicator readings for 10 trials conducted to measure accuracy in motion for LH-Wrist, RH-Wrist, Both wrists combined, and 4-DOF Robot Arm.

replacing the composite with plastic panels. The numerical methods [23], [24] is essential to optimize the design of the panel for making the arm lighter. The grippers with suction [25] or soft/hybrid fingers from our previous works [26], [27] will be attached to the wrist to grip the objects. The artificial skin [28] can be covered outside the robot hand for sensing and friendly interaction.

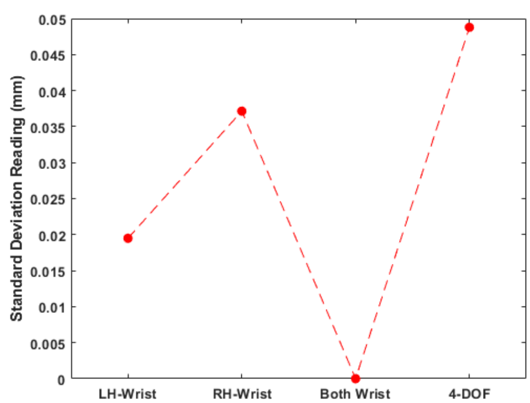

Fig. 13. Graphical illustration showing Standard Deviation readings for each set of experiments conducted at LH-Wrist, RH-Wrist, Both wrists combined and 4-DOF Robot Arm.

IV. Conclusions

This study proposed a novel design of the 5 DOF cable-driven robot arm which can lift 5 kg load hooked at the 700 mm distance from the shoulder center. Additionally, the accuracy in operating for the wrist and the arm were less than 1 mm. Such achievements were obtained thanks to optimizing the weight of the robot frame by combining the counterbalance design. Also, the decoupling mechanism and the elbow design increase the stability of the wrist and the arm during operation.

Acknowledgment

This research is supported by the Agency for Science, Technology and Research (A*STAR) under its IAF-ICP Programme I2001E0067 and the Schaeffler Hub for Advanced Research at NTU. Also, Nguyen was a postdoc research fellow at School of Materials Science, Japan Advanced Institute of Science and Technology where he was fully supported by Japan Society for Promotion of Science (JSPS PD) and JSPS Kakenhi Grants No 20J14910.

References

[1] G. D. Goh and H. Alvin, “3d printing of robotic soft grippers: Toward smart actuation and sensing,” *Adv. Mater. Technol.*, vol. 1, no. 11.
[2] P. V. Nguyen, “Towards safely grasping group objects by hybrid robot hand,” in *2021 4th International Conference on Robotics, Control and Automation Engineering (RCAE)*, 2021, pp. 389–393.
[3] J. Hernandez and M. H, “Current designs of robotic arm grippers: A comprehensive systematic review,” *Robotics*, vol. 12, no. 1, 2023.
[4] P. V. Nguyen and V. A. Ho, “Grasping interface with wet adhesion and patterned morphology: Case of thin shell,” *IEEE Robotics and Automation Letters*, vol. 4, no. 2, pp. 792–799, 2019.
[5] V. P. Nguyen and W. T. Chow, “Towards flexible manipulation with wiring-base robot hand,” in *Robot Intelligence Technology and Applications 7*. Springer International Publishing, 2023, pp. 385–392.
[6] S. Yang and S. Xu, “Accuracy of autonomous robotic surgery for single-tooth implant placement: A case series,” *Journal of Dentistry*, vol. 132, p. 104451, 2023.
[7] B. N. Staub, “The use of robotics in minimally invasive spine surgery,” *Journal of Spine Surgery*, vol. 5, no. Suppl 1, 2019.
[8] R. J. Trute and M. Suphi, “Development of a robotic surgery training system,” *Frontiers in Robotics and AI*, vol. 8, 2022.
[9] Https://www.universal-robots.com/products/ur5-robot/.
[10] Https://new.abb.com/products/robotics/robots/articulated-robots.
[11] Denso robot https://www.densorobotics.com/.
[12] Https://www.kuka.com/en-sg/products/robotics-systems.
[13] FANUC product https://www.fanuc.com/product/index.html.
[14] H. Wang, “Performance investigation of cone dielectric elastomer actuator using taguchi method,” *Chin. J. Mech. Eng.*, vol. 24, 2011.
[15] Y. Xu, “Path planning and intelligent control of a soft robot arm based on gas-structure coupling actuators,” *Front. Mater.*, vol. 9, 2022.
[16] P. Rao, Q. Peyron, S. Lilge, and J. Burgner-Kahrs, “How to model tendon-driven continuum robots and benchmark modelling performance,” *Frontiers in Robotics and AI*, vol. 7, 2021.
[17] Z. Gong and L. Wen, “An opposite-bending-and-extension soft robotic manipulator for delicate grasping in shallow water,” *Frontiers in Robotics and AI*, vol. 6, 2019.
[18] H. t. Su, “Pneumatic soft robots: Challenges and benefits,” *Actuators*, vol. 11, no. 3, 2022.
[19] S. t. Qian, “A review on cable-driven parallel robots,” *Chinese Journal of Mechanical Engineering*, vol. 31, 2018.
[20] G. Lum and S. Yeo, “Design and motion control of a cable-driven dexterous robotic arm,” in *2010 IEEE Conference on Sustainable Utilization and Development in Engineering and Technology*, 2010.
[21] S.-R. Oh and S. Agrawal, “Cable suspended planar robots with redundant cables: controllers with positive tensions,” *IEEE Transactions on Robotics*, vol. 21, no. 3, pp. 457–465, 2005.
[22] K. Choi and F. C. Park, “A hybrid dynamic model for the ambidex tendon-driven manipulator,” *Mechatronics*, vol. 69, p. 102398, 2020.
[23] W. T. Chow and M. Graves, *Stress analysis of a rectangular implant in laminated composites using 2-D and 3-D finite elements.*
[24] T. N. Nguyen, “Load-carrying capacity of ultra-thin shells with and without cnts reinforcement,” *Mathematics*, vol. 10, no. 9, 2022.
[25] J. Courchesne and P. Abdoul, “A compact underactuated gripper with two fingers and a retractable suction cup,” *Frontiers in Robotics and AI*, vol. 10, 2023.
[26] P. V. Nguyen and V. Ho, “Wet adhesion of micro-patterned interfaces for stable grasping of deformable objects,” in *2020 IEEE/RSJ International Conference on Intelligent Robots and Systems (IROS)*, 2020, pp. 9213–9219.
[27] V. P. Nguyen and W. T. Chow, “Wiring-claw gripper for soft-stable picking up multiple objects,” *IEEE Robot. Autom.*, pp. 1–8, 2023.
[28] P. Van Nguyen and V. A. Ho, “Toward a tactile ontology for semantic interoperability of the tactile internet,” in *2022 IEEE 16th International Conference on Semantic Computing (ICSC)*, 2022, pp. 115–118.